Accuracy of polarization field measurements by electron holography in InGaN quantum wells

T. Niermann,* L. Niermann, M. Narodovitch, and M. Lehmann
Technische Universität Berlin, Straße des 17. Juni 135, Berlin, Germany

(Received 9 September 2020; revised 23 November 2020; accepted 3 February 2021; published 18 February 2021)

We thoroughly investigate two methods for estimating electric field strength across semiconductor heterostructure quantum wells from electron holograms. Due to the small width of quantum wells these holograms must often be taken under dynamical diffraction conditions, since projection effects forbid the investigation under larger tilt angles. We especially investigated the robustness of the evaluation methods against dynamical diffraction artifacts due to excitation conditions and strain, artifacts due to the material contrast, as well as limited resolution effects. For this we developed ways to incorporate polarization effects into combined strain and multislice simulations. It turns out that errors estimated from detection noise of single measurements alone mostly underestimate the true error, since variation due to hardly controlled diffraction effects and measurement details often prevails.

DOI: 10.1103/PhysRevB.103.075306

I. INTRODUCTION

The electronic and optoelectronic properties of wurtzite-phase group-III nitride heterostructures are strongly affected by the spontaneous and piezoelectric polarization along the c axis of these compounds. The polarization strength depends nonlinearly on composition and strain state within these multilayer structures [1,2]. Abrupt changes in polarization at internal interfaces cause large internal electrostatic fields and interfacial sheet charges. In quantum wells (QWs) of light-emitting diodes and laser diodes this causes the quantum confined Stark effect, mostly observable as a reduction of the radiative recombination rate together with a redshift of the emission wavelength [3–5]. For high-electron-mobility transistors the strong band bending caused by the interfacial charges is even beneficial for device performance [6].

Measuring the strength of these internal fields directly is a formidable task, since it requires a method capable of quantitative electric field measurements on the nanometer scale. Electron holography (EH) within the transmission electron microscope (TEM) is such a measurement technique. It allows to measure the mutual phase shift of two electron waves which traveled along different paths [7]. If one path goes through the specimen and the other through vacuum, the observed phase shift is proportional to the projected electrostatic potential within the specimen. This at least is true in the simple picture of kinematic electron diffraction. Several examples of electron holographic measurement of such fields in group-III nitride structures can be found in the literature [8–17].

In order to mitigate the influences of surface effects like strain relaxation, surface damage, and band bending due to surface defects ("dead layers") [18–21], typically specimens of a few hundred nanometers' thickness are investigated. Thicker specimens additionally provide a more significant phase signal. However, thicker specimens require that for avoidance of projection effects the typically only few-nanometer-wide QW must be oriented on edge. On the other hand, the on-edge orientation corresponds to strong diffraction conditions (here systematic row conditions) [9,13,22], where the assumption of kinematic diffraction breaks down. Also the different materials cause diffraction effects at the interface. Additionally, the surface relaxation of the strain within the thin specimen lamella results in diffraction conditions that are changing over the specimen thickness. In some publications (e.g., in Ref. [9]) these effects are qualitatively discussed as a source of error; however, no efforts have been undertaken so far to quantify their influence on the measurement accuracy.

The avoidance of surface effects also requires that the investigated structures are not too close to the specimen edges. This requires distances between both holographically interfered paths (overlap), typically in the range of hundreds of nanometers. Typically, the TEM is operated using the Lorentz lens for such observations, as the low magnification of the Lorentz lens is the only way to allow such large path differences in common TEM setups. However, the relative strong aberrations of the Lorentz lens limits the spatial resolution of such measurements typically to above 2 nm. Obviously, observing an electric field in a QW, which has a similar width as the resolution of the microscope, will become an additional source of inaccuracy for such a measurement.

Most reports of electric field measurements of QW in group-III nitrides in the literature cover different heterostructures, which makes them not comparable. Nevertheless, several reports exist for 2- to 3-nm-wide $In_cGa_{1-c}N$ QWs within a GaN matrix for In concentrations in the range $c = 0.13, \ldots, 0.18$: Haas *et al.* [17] report values of the electrical field strength within several (2.2 ± 0.2)-nm-wide $In_{0.15}Ga_{0.85}N$ QWs between 3.3 and 3.8 MV/cm (± 0.2 MV/cm) measured by means of EH and values between 2.2 and 3.7 MV/cm (± 0.2 MV/cm) for differential

*tore.niermann@tu-berlin.de

 ©2021 American Physical Society

phase contrast (DPC) measurements performed on the same sample. Stevens *et al.* [12] report field strength of 1.65 ± 0.6 MV/cm (values taken from figure) for a 2-nm-wide $In_{0.13}Ga_{0.87}N$ QW (measured by EH). Cai and Ponce report 2.2 ± 0.6 MV/cm for a 2.7-nm-wide $In_{0.18}Ga_{0.82}N$ QW (also EH) [11]. Theoretical predictions for the field strength are in the range of 2.2 MV/cm (for $c = 0.13$ [1]). Overall, a large spread of the reported values for holographic electric field measurements is already noticeable in the literature.

We present a systematical quantitative investigation on the accuracy of the electron holographically measured field strength. For this we perform combined strain and multislice simulations. We developed and discuss two ways to include the effect of polarization fields into such simulations. For the calculated electron exit waves we test and discuss the robustness of different methods of field strength evaluation under the present dynamical diffraction conditions and especially focus on the influences to experimental conditions like incident beam tilt and limited resolution.

II. METHODS

For our calculations we model the specimen that was investigated in the article of Haas *et al.* [17]: the heterostructure consisted of six 2.25-nm-wide $In_{0.15}Ga_{0.85}N$ QWs separated by 12-nm GaN layers and followed by an 80-nm-thick GaN layer on top of the QW stack. The growth direction was the GaN-[0001] direction (Ga polar surface). We assumed the thickness of the investigated specimen lamella to be in the range between 200 and 240 nm. This is within the optimal thickness range for EH measurements on GaN at 300 kV acceleration voltage, given that for silicon 200–400 nm is an optimal thickness range [18] and GaN is a heavier compound.

A. Strain simulations

The specimen was modeled in a continuum model of the layered heterostructure, where a displacement field describes changes of the lattice relative to a relaxed GaN lattice. The used material constants were taken from literature [23–29] and are listed in Table S1 of the Supplemental Material [30]. For the $In_{0.15}Ga_{0.85}N$ layers the constants were linearly interpolated between the GaN and InN values according to Vegard's law.

For tests of the implementations of the polarization field (see below), the pseudomorphic strain model was applied. It assumes that the InGaN layers have the same in-plane (basal plane) lattice constants as the GaN matrix. This model includes the biaxial strain occurring due to the misfit; i.e., the displacement field adjusts the lattice constants of the quantum well such that [31]

$$a_{QW} = a_{GaN} \quad \text{and} \quad c_{QW} = c_{InGaN}\left(1+2\frac{C_{13}}{C_{33}}\frac{a_{InGaN}-a_{GaN}}{a_{GaN}}\right). \tag{1}$$

Strictly speaking this pseudomorphic model is only valid for an infinitely large specimen, since relaxation effects at the specimen surface will occur. Since strain relaxations at the surface will strongly influence the dynamical scattering behavior of the specimen, these relaxations were also considered in the final simulations, where the continuum displacement field was obtained by the finite-element method (FEM) using linear elasticity theory. The strained layers were modeled by the concept of Eshelby's inclusions [32]. The method is described in more detail in Ref. [33]. The displacements were calculated for several lamellas with thicknesses between 200 and 240 nm. The calculations were done for a three-dimensional specimen slab. In the growth direction as well as in the electron beam direction the specimen has a constricted size in the experiment. In the remaining direction the specimen is sufficiently large to neglect any surface effects. The slab used for strain calculation was 1 μm wide in this direction and any of the displacements entering the subsequent scattering modulations were evaluated in the center of the slab. The slab featured a 361-nm-wide GaN substrate, which was fixed to zero displacement at its bottom side. The resulting displacement field is depicted in Fig. S1 of the Supplemental Material [30].

B. Scattering simulations

The multislice simulations require an atomic model of the specimen, which was obtained from the continuum model in the following way. A large supercell with 36 GaN unit cells in the c direction and a beam direction corresponding to the GaN $[\bar{4}\,11\,\bar{7}\,0]$-zone axis was created. This zone axis was chosen because it is sufficiently close to (0002) systematic row conditions while simultaneously allowing a periodic supercell along the remaining direction. This perpendicular periodicity corresponds to the $[6\,\bar{1}\,\bar{5}\,0]$ GaN lattice vector. The size of the supercell in the beam direction was made large enough to accommodate the full thickness of the lamella. The supercell was populated by Ga and N atoms corresponding to the respective sites of the enclosed GaN lattice. Subsequently, the atoms which are positioned within a QW region of the continuum model were marked specially. For the N atoms in the QW the relative displacement to the Ga atoms was adjusted according to the interpolation formula given by [1]

$$u(c) = 0.3793c + 0.3772(1.0 - c) - 0.0057c(1.0 - c),$$

with an indium concentration of $c = 0.15$. Finally, all atom positions were displaced according to the continuum displacement model. Since the continuum model is much larger than the supercell, the supercell only captures the region around one QW of the continuum model. In all presented simulations the displacements around the bottom QW of the multi-QW stack were used.

Electron beam propagation through the atomic model was simulated for 300-keV electrons using the multislice method [34] on a grid of 1536×256 points, resulting in a sampling of 12.1×12.0 pm/pixel. In the propagation steps, a cutoff at 27.5 1/nm (54 mrad) was used. The atomic model was separated into 0.15-nm-thick slices and the atomic potential of all atoms within each slice was projected. For the atomic potential the parametrization of Kirkland [35] was used. For the metal sites within the QW, a linear interpolation between the parametrized atomic potentials of Ga and In was used.

The complex-valued electron wave front emanating from the multislice simulation was Monte Carlo averaged over 30 samples of atomic positions disturbed according to the

thermal displacement parameters of the respective atom (see Table S1 [30]) in order to incorporate thermal diffuse scattering effects [36,37].

The resulting wave fronts were averaged in the direction perpendicular to the GaN's c axis. The resulting profiles were subsequently Fourier filtered with a Gaussian modeling the microscope's envelope, the mask used in the experimental holographic reconstructions, and a sinc filter corresponding to a subsequent rebinning of the values. Unless otherwise noted, we used the experimental conditions found in the FEI Titan 80-300 "Berlin Holography Special" microscope for this. Typically the (0002) reflections are barely visible within experimental holograms under aberration-corrected conditions, when simultaneously a wide hologram overlap of around 230 nm is used to avoid effects of the specimen edges.

Using q as scattering vector, the microscope's envelope is modeled as

$$f(q) = \exp(-2q^2 d_{(0002)}^2)$$

such that the envelope reaches $\exp(-2)$ at the (0002) reflection, which corresponds to a resolution limit at $d_{(0002)} = 0.259$ nm. A reconstruction cutoff of 4.5 1/nm was used to let these reflections pass, and a 14th-order Butterworth filter was chosen to soften the mask's edges. Finally, a sinc filter

$$f(q) = \mathrm{sinc}(bq)$$

with $b = 0.345$ nm was applied, which corresponds to typical bin sizes b in experimental profiles.

All electron beam simulations were performed using the PYTEM software package [38] and 300 kV acceleration voltage. Due to the nature of the discrete Fourier transforms used within the multislice algorithm and the subsequent filtering, the simulated profiles are continuous and periodic at their boundaries. However, the corresponding faces of the supercell are placed at arbitrary positions. This results in wraparound artifacts in the calculations (see for instance Fig. 2). For this reason we treat the left- and rightmost 3 nm of the calculated profiles as artifacts without further consideration.

C. Modeling polarization fields in simulations

A comprehensive modeling of the electrostatic potential within the specimen requires the calculation of the (valence) electron density in order to fully incorporate bonding, band offset, and polarization effects, which can be in principle achieved by, e.g., density functional theory [1]. Since our aim here is an investigation of occurring artifacts and the robustness of evaluation strategies against these artifacts, it is sufficient to approximate the resulting electrostatic potential. For this we adopt the commonly used isolated atom approximation to model the potential in both materials, as already implicitly indicated by the use of the atom form factors above.

However, no approaches for the incorporation of polarization effects into electron microscopic simulations exist. We tried two approaches for the incorporation of the polarization, a more microscopic one, where additional charges were modeled on the atom positions, and a macroscopic one, where only interfacial charges were added.

In the microscopic picture, the spontaneous and piezoelectric polarization of the group-III nitrides occurs due to the partial ionic nature of the atomic bonding together with the deviation from the ideal tetrahedral coordination [39]. The partial ionic nature can be quantified by an effective charge of the atomic sites, which represents the effective number of valence electrons close to the nuclei [28]. We subtract the number of electrons needed for the neutral atom (i.e., five for nitrogen, three for the metal atom) from this effective charge to form effective excess charges: $Q = 1.02e$ for the Ga atom in GaN and $Q = 1.04e$ for the metal atoms in $In_{0.15}Ga_{0.85}N$. The N atom has the same effective charge but is of opposing sign for each compound. We incorporated this excess charge Q into our calculations by adding the pseudoatom form factor resulting from a Gaussian charge distribution centered on the atom site to the atom form factor $f_{\mathrm{Neutral}}(q)$ of the neutral atom,

$$f_{\mathrm{Ion}}(q) = f_{\mathrm{Neutral}}(q) + \frac{em_0}{2\pi\epsilon_0 h^2}\frac{Q}{q^2}\exp\left(-2\pi^2 R_{\mathrm{ff}}^2 q^2\right) \quad \text{for } q \neq 0. \tag{2}$$

Here e is the elementary charge, m_0 is the electron rest mass, h is Planck's constant, and q is the scattering vector. R_{ff} is the root-mean-square (rms) width of the Gaussian distribution, which still must be adjusted to the simulation. For $q = 0$ the neutral form factor was left unchanged, which results in an overall electrically neutral supercell.

In Fig. 1 the difference between the potential calculated with the modified form factor $f_{\mathrm{Ion}}(q)$ and the unmodified form factors $f_{\mathrm{Neutral}}(q)$ is shown. The depicted potential was averaged over the specimen thickness, as internally only the projected potential is calculated. In order to make the potential in the figure more illustrative, here only the strain of a pseudomorphically strained QW [as given by Eq. (1)] was assumed as well as the atomic potential being smoothed by the Debye-Waller factor, while the final simulations were done for the strain state calculated by the finite element method, which includes surface relaxation effects, and with the Monte Carlo integration of thermal displacements. It can be seen that the resulting macroscopic electrical fields are rather independent of the choice of R_{ff}. But it becomes apparent that for a too-small choice of R_{ff} (e.g., for $R_{\mathrm{ff}} = 0.10$ nm) the structure factors become significantly changed, since here an additional modulation with the monolayer period appears. This microscopic approach to polarization modeling mimics the true microscopic source of the polarization fields and already creates interfacial charges. However, it also creates an artificial charge dipole at the periodic supercell boundary. These boundary charges would not appear if the size of the supercell is an integer number of unit cells. However, when surface relaxations are later included in the simulation, it becomes impossible to create such a commensurable supercell. Furthermore, the microscopic model also lacks the incorporation of the electric susceptibility. Since these artificial boundary charges caused too-strong diffraction artifacts for the chosen supercell sizes and due to the fact that different polarization field strengths and susceptibility must be modeled quite artificially by changing the effective charge strength between both materials, we selected a different way of modeling the polarization fields.

In a macroscopic picture, changes of the polarization are observable as charges. For a heterostructure like here, these

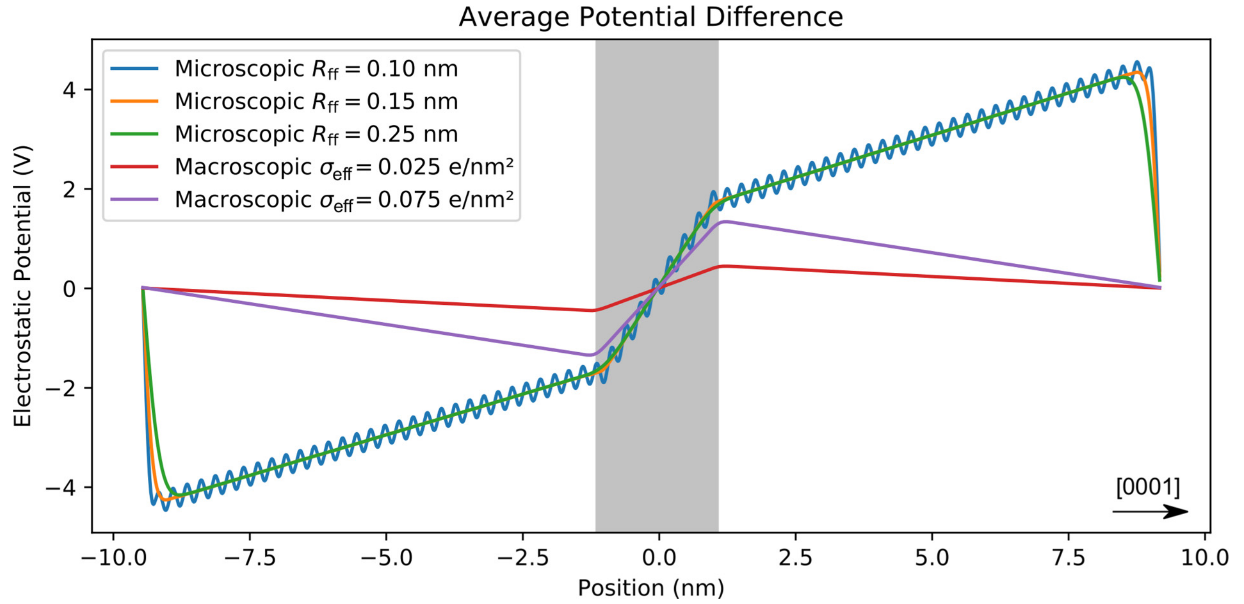

FIG. 1. Difference between the electrostatic potential with and without included polarization effects (averaged over specimen thickness). The "microscopic" model utilizes modified form factors as given by (2). The "macroscopic" model included the potential resulting from additional interfacial charges as given by (4) instead. The region of the QW is marked by the gray background; its center is located at the zero position. The charges induced by the polarization effects are shown in Fig. S1 of the Supplemental Material [30].

charges occur mainly as sheet charges σ_{eff} at the interfaces between the materials due to changes in spontaneous P^{sp}, piezoelectric polarization P^{pz}, as well as induced (dielectric) polarization. The resulting electric field is given by [1]

$$E_{\text{QW}} = -\frac{\sigma_{\text{eff}}}{\epsilon_0} = \frac{1}{\epsilon_0\left(\kappa_{\text{In}_{0.15}\text{Ga}_{0.85}N} - 1\right)} \times \left[\left(P^{\text{sp}}_{\text{GaN}} + P^{\text{pz}}_{\text{GaN}}\right) - \left(P^{\text{sp}}_{\text{In}_{0.15}\text{Ga}_{0.85}\text{N}} + P^{\text{pz}}_{\text{In}_{0.15}\text{Ga}_{0.85}N}\right)\right]. \quad (3)$$

Since the piezoelectric polarization is primarily caused by the pseudomorphic strain within the QW, any additional piezoelectric polarization changes due to relaxation effects at the surfaces are neglected. Please note that the definition of effective sheet charges σ_{eff} used in (3) includes the charges due to the induced dielectric polarization and thus differs by the electric susceptibility $\kappa - 1$ from the sheet charges occurring due to changes in spontaneous and piezoelectric polarization alone. The sheet charge σ_{eff} is specified for the upper interface ($x > 0$).

In the macroscopic approach for modeling the polarization fields these interfacial charges are explicitly added to the simulations. For this, the location of the interfaces r_{if} in the growth direction was sampled with 1-nm-depth resolution from the continuum model. At these positions the electrostatic potential $V_{\text{if}}(r - r_{\text{if}})$ resulting from a sheet charge distribution, which is smoothed out by a Gaussian with rms width R_{if} in the growth direction, is added to the potential of each multislice slice:

$$V_{\text{if}}(r) = \frac{\sigma_{\text{eff}}}{4\pi^2\epsilon_0}\int_{-\infty}^{+\infty} dq\, \frac{\exp(-2\pi^2 R_{\text{if}} q^2)}{q^2} \exp(i2\pi q r). \quad (4)$$

This interfacial charge potential was added for both interfaces with opposing sign of the sheet charge, such that the overall supercell remains electrically neutral again. The Gaussian smoothing here should avoid high spatial frequencies and is set to $R_{\text{if}} = 0.15$ nm for all simulations. Using this macroscopic approach to model the polarization fields allows to directly specify the interfacial sheet charge σ_{eff} for the simulation.

Figure 1 shows the difference of the thickness-averaged potential between supercells with and without interfacial charges. Due to the artificial boundary charges of the microscopic model, the potentials obtained for both approaches differ by an additional electric field stretching over the whole supercell. However, this additional electric field will not change the result of any (sensible) further data evaluation method: Additional global electric fields (as well as an additive constant potential) are only determined by the electric boundary conditions of the experiment. Since these boundary conditions are usually not sufficiently well defined in the experiment (see discussion in Sec. IV), any evaluation methods of polarization field from holographic measurements should be insensitive to these contributions anyway.

We want to use the simulations to test whether the field strength obtained by the evaluation methods described in the next section agree with the field strengths assumed for the simulation itself, i.e., whether the methods are truthful. For illustration purposes we mainly assume a sheet charge of $\sigma_{\text{eff}} = 0.025e/\text{nm}^2$ in the following, which corresponds to an electric field strength of -4.5 MV/cm. The reported values for the expected electric field strength vary in the literature, as discussed in the Introduction. However, they are always in this order of magnitude. The effective charges used in the microscopic method above correspond to a sheet charge of $\sigma_{\text{eff}} = 0.075e/\text{nm}^2$. They were taken from [28], but significantly different values for the effective charges can also be found in the literature (e.g., in Ref. [40]). *Ab initio*

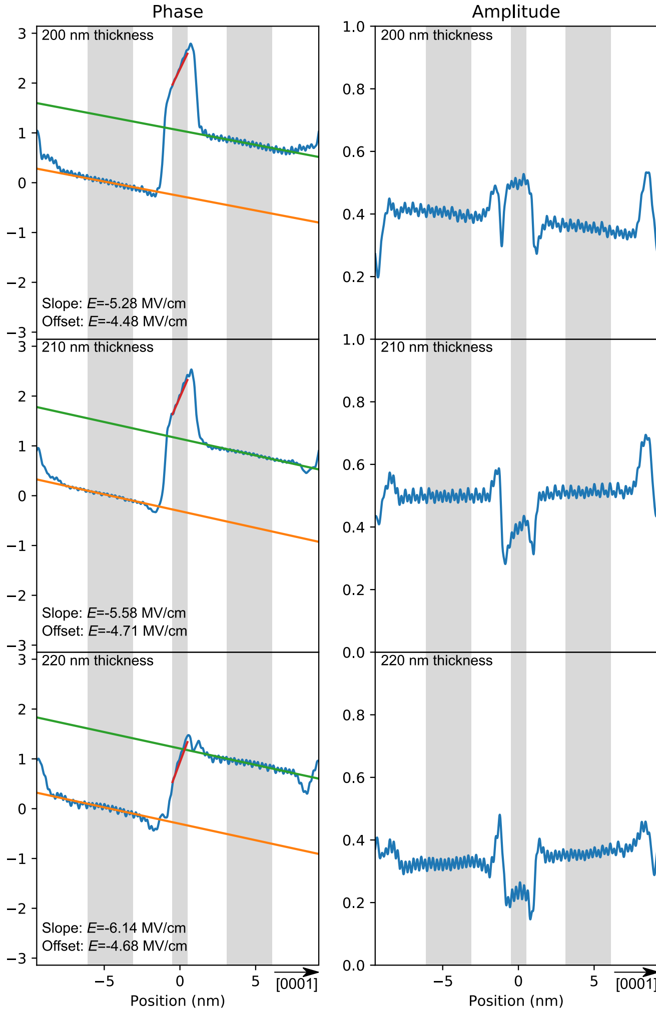

FIG. 2. Simulated profiles for 200-, 210-, and 220-nm-thick lamellas at zero tilt with interfacial charge densities of $\sigma_{\mathrm{eff}} = \pm 0.025\, e/\mathrm{nm}^2$. Within the phase profile the orange and green lines mark the gradients and offsets estimated from the matrix regions to the left- and right-hand sides of the QW underlaid by the gray background. The red line indicates the gradient estimated within the center of QW. The underlaid gray mark in the QW center marks the $-\delta < r < \delta$ interval for this center gradient estimation (see main text). The field strength obtained from both estimators is noted in the lower left corner of the phase plots.

calculations expect a field strength of $E_{\mathrm{QW}} = -2.2\,\mathrm{MV/cm}$ for an $In_{0.13}Ga_{0.87}N$ QW in a GaN matrix (under the assumption of no further screening by free carriers) [1], which corresponds to $\sigma_{\mathrm{eff}} = 0.012 e/\mathrm{nm}^2$. Also, when the expected polarization is evaluated for a pseudomorphically strained InGaN with the theoretical polarization constants given in Refs. [41,42], values of similar magnitude are obtained.

D. Estimation of electric field strength within the quantum well

Simulated profiles for lamellas of several thicknesses at zero tilt, $\tau = 0$ mrad, for an interfacial charge density of $\sigma_{\mathrm{eff}} = +0.025\, e/\mathrm{nm}^2$ are shown exemplarily in Fig. 2. Clearly observable is the position of the QW in the amplitude profile from $-1.0 \lesssim r \lesssim 1.0$ nm. In the region of the QW an increasing phase profile is observable. Also observable are identical phase gradients in the matrix regions to the left- and right-hand sides of the QW. The slight high-frequency wiggling of the profiles is the remaining lattice contrast from the $\pm(0002)$ reflections.

The "slope" method evaluates the gradient of the phase within the QW directly. In the simple kinematic picture, where the phase $\varphi(r)$ is proportional to the projected electrostatic potential

$$\varphi(r) = C_E t V(r), \tag{5}$$

with lamella thickness t, electrostatic potential $V(r)$, and the acceleration voltage-dependent interaction constant [7] $C_E = 6.52 \times 10^{-3}$ rad/(V nm), these phase gradients in the QW and the surrounding matrix can be interpreted as electric fields:

$$E_{\mathrm{Slope}}(r) = -\frac{dV}{dr} = -\frac{1}{C_E t}\frac{d\varphi}{dr}.$$

As discussed in Sec. II C, the electric fields are also depending on the boundary conditions; thus only the difference of the potential gradients of the QW and matrix can be interpreted as a polarization field:

$$E_{\mathrm{QW}} = E_{\mathrm{Slope}} - E_{\mathrm{Matrix}} = -\frac{1}{C_E t}\left[\left.\frac{d\varphi}{dr}\right|_{\mathrm{QW}} - \left.\frac{d\varphi}{dr}\right|_{\mathrm{Matrix}}\right]. \tag{6}$$

In the following we refer to (6) as the "slope" method for estimation of the field strength. Examples for the use of such an estimator are Refs. [14,15,17].

The "offset" method evaluates a second quantity, which also depends on the polarization field strength E_{QW} within the QW. The potential difference between the regions to the left (at r_{L}) and right (at r_{R}) sides of the QW depends on the field strength E_{QW} within the QW, its width w, and the field strength E_{Matrix} in the matrix:

$$V(r_{\mathrm{R}}) - V(r_L) = wE_{\mathrm{QW}} + (r_R - r_L)E_{\mathrm{Matrix}},$$

thus

$$E_{\mathrm{QW}} = -\frac{1}{wC_E t}\left[\varphi(r_R) - \varphi(r_L) - \left.\frac{d\varphi}{dr}\right|_{\mathrm{Matrix}}(r_R - r_L)\right]. \tag{7}$$

In the following we refer to (7) as the "offset" method for estimation of the field strength. Examples for the use of such an estimator are Refs. [9,10,13].

Both methods (6) and (7) depend on phase values or gradients of the phase values, which are quantities subjected to noise in the measurement. Furthermore, the calculation of the phase from the complex-valued hologram reconstructions is a nonlinear operation. This nonlinearity leads to a phase variance, which is inversely proportional to the amplitude [43,44]. The noise dependency is considered by Gaussian error propagation. For a robust estimation, these phase values and gradients are additionally averaged over a region of the profile.

Assuming the center of the QW is located at $r = 0$, the phase values $\varphi(r_L)$ were averaged within the interval $-6.1 \leqslant r \leqslant -3.1$ nm and the phase values $\varphi(r_R)$ within the interval $3.1 \leqslant r \leqslant 6.1$ nm, and the positions r_L and r_R were taken in the center of the intervals. The phase gradients of the GaN matrix were estimated in both aforementioned intervals simultaneously. The phase gradient within the QW was evaluated

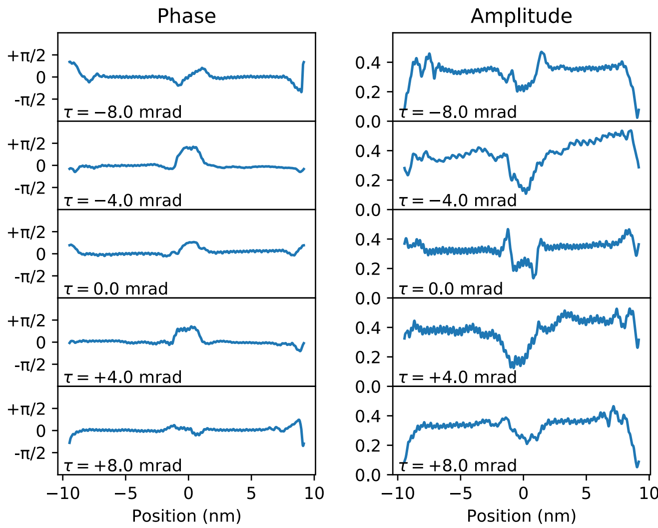

FIG. 3. Phase and amplitude profiles from simulations for a 220-nm-thick specimen, a QW width of 2.25 nm, and no additional interface charges for various tilts.

using a weighted average, with a Gaussian centered at $r = 0$ and with $\delta = 0.50$ nm rms width as a weighting envelope. The detailed equations used for the evaluation can be found in the Supplemental Material [30].

These intervals and the $-\delta \leqslant r \leqslant +\delta$ interval in the Gaussian weighted case are also depicted in Fig. 2 together with the evaluated phase gradients and offsets as well as the estimated field strengths using both methods. It should be noted that, even though the QW gradient region seems off center in the phase profile, this region actually is centered in the amplitude profile. However, the exact positioning of the QW center is a systematic error source, as we discuss later.

E. Evaluation of interfacial charges from second derivative

In the literature, also uses of the second derivative of the reconstructed phase for the estimation of field strength or more exactly the estimation of interfacial charges can be found (e.g., Refs. [8,11,45]). This estimation is based on the Poisson equation and gives a charge distribution $Q(r)$ within the kinematic picture of (5):

$$Q(r) = -\epsilon_0 \Delta V\bigg|_r = -\frac{\epsilon_0}{C_E t}\Delta\varphi\bigg|_r. \tag{8}$$

This charge can be evaluated at the interface of the QW and GaN matrix. We here rejected this evaluation method for several reasons:

First, at the interface between QW and GaN also the interfacial charge dipole responsible for the difference of the mean inner potential between both materials is located. However, neither is there a reason for this charge dipole to be exactly asymmetrical around the interface nor a symmetrical propagation of the wave within the sample can be assumed, due to projection and dynamical diffraction effects. This nonsymmetrical interface can be immediately noticed in the simulated phase profiles in Fig. 3, where no polarization field is added to the calculation. Nor is there a reason to assume that both interfaces are symmetric with each other. This nonsymmetry between both interfaces can also be observed in Fig. 3.

The effect of a nonasymmetrical dipole charge distribution can be avoided, when the charge (8) is not evaluated at a single position but integrated over the whole interfacial area I:

$$Q_{\text{Total}} = \frac{1}{I}\int_I dr\, Q(r).$$

Since the interfacial dipole is created by two opposing charges, its contribution to Q_{Total} should vanish and only the interfacial charge due to changes in the polarization should remain. When (8) is only evaluated at a single point, it is not obvious how this interfacial dipole can be separated from the interfacial charge, nor how to place this point in experimental data, where the exact position of the interface is unknown.

Second, in the general case the second derivative is biased in cases of limited resolution. This becomes immediately obvious when the second derivative of (8) is evaluated in Fourier space,

$$Q(r) = \frac{4\pi^2\epsilon_0}{C_E t}\int_{-\infty}^{+\infty} dq\, q^2\tilde{\varphi}(q)\exp(i2\pi qr), \tag{9}$$

using the Fourier-transformed phase

$$\tilde{\varphi}(q) = \int_{-\infty}^{+\infty} dr\, \varphi(r)\exp(-i2\pi qr).$$

When higher frequencies q are attenuated, e.g., the integral in (9) is only evaluated in the limits of $-q_{\max} < q < q_{\max}$, but $\tilde{\varphi}(q)$ does not vanish for $|q| > q_{\max}$, the resulting evaluated charge Q becomes biased. This bias remains even when the charge is integrated over the interfacial area. A truthful evaluation of the charge thus requires that the resolution of the holographic reconstruction is sufficiently smaller than the extent of the interfacial charge.

Third, while the numerical evaluation of the first derivative already increases the variance by a factor of 2 compared to the original signal, the variance of the numerically evaluated second derivative becomes even four times larger than the original signal.

III. RESULTS

Systematical tilt and thickness variations are used to investigate the combined effects of strong diffraction, projection artifacts, and difference in material. Observed variations and the bias of the estimators are statistically quantified.

The effect of beam tilt alone with a tilt axis parallel to the interfaces on the calculated profiles without added polarization fields can be seen exemplarily in Fig. 3 for a specimen thickness of 220 nm. It is obvious that the shape of the profile across the QW and especially the shape of the interfaces is dependent on the beam tilt. Also visible are slight oscillations of the phase profiles in the center of the QW, which may complicate the evaluation of a slope in these parts. In general also the width of the apparent QW becomes wider when the beam is tilted away from the zero position. This is expected due to projection effects.

The effect of the interfacial charges occurring due to changes in the polarization between both materials is displayed in Fig. 4. Clearly observable is the increase of the phase gradient with increasing interfacial charge, as well as an increase of the phase step between both sides of the QW. Indeed, the effect of the interfacial charge on the phase is

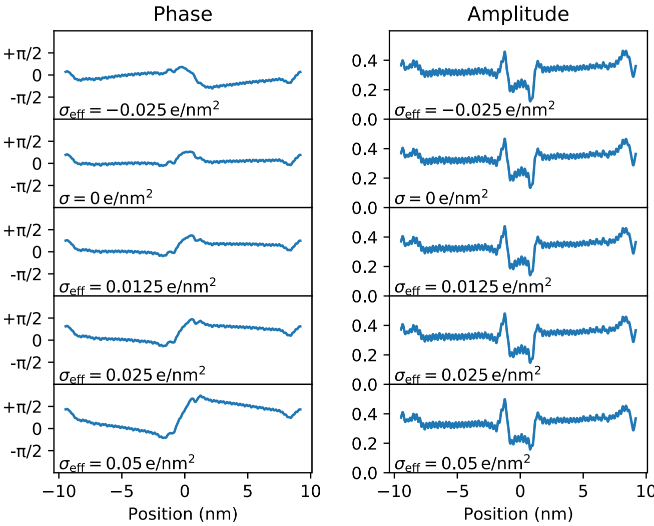

FIG. 4. Phase and amplitudes from simulations for a 220-nm-thick specimen at zero tilt for various interfacial charge densities $\sigma_{\rm eff}$.

found to be interpretable as an additive effect in the simulated range of thicknesses and beam tilts. Also, the additional electrostatic field is too weak to have a significant influence on the amplitudes.

The electric field strengths estimated by slope estimator (6) and the offset estimator (7) using calculated profiles for an interfacial charge of $\sigma_{\rm eff} = 0.025e/{\rm nm}^2$ are shown in the left column of Fig. 5. The estimates were evaluated for a tilt range from −8.45 to +8.45 mrad and thicknesses from 200 to 240 nm. The expected field strength for the homogeneous field between both interfaces is $E_{\rm QW} = -\sigma_{\rm eff}/\epsilon_0 = -4.524$ MV/cm. Exemplarily the estimates for 220-nm thickness are also shown as line graph in the bottom row.

The right column of Fig. 5 shows the expected standard error of the obtained field strength for each tilt and thickness. Assuming the detection noise is Poisson distributed, the variance of each data point in the reconstructed hologram will be proportional to the point's amplitude, while the proportionality factor will depend on the electron dose and the detector. The errors for each individual field estimation displayed in Fig. 5 are obtained by Gaussian error propagation from the noise in the reconstructed data points. Any correlations introduced by the reconstruction aperture and the rebinning were considered by performing the error propagation with the full covariance matrix (see Ref. [44] for details of error propagation of holographic reconstructions). Since there is a constant global factor depending on dose and detector in the experiment, the presented errors are only given in arbitrary units. Nevertheless, they are comparable among each other.

A wide range of field estimates is found for both estimators; however, the evaluated value varies far more for the slope estimator. The strongest deviations in Fig. 5 are found for tilt and thickness combinations, where the intensity of the zero beam of the electron wave is small either in the QW itself or in the matrix (also see Fig. S3 of the Supplemental Material [30]). These small intensities occur due to dynamical diffraction effects.

When the standard deviations of the estimators are compared with the field estimations, i.e., the left and right columns of Fig. 5 are compared, it becomes obvious that most of the large deviations found are caused by these low intensities. In order to quantify the spread of the estimated field strength due to the experimental conditions, we calculated the weighted averages and standard deviations over the shown tilt and thickness ranges. The inverse square of the presented standard errors were taken as weights. The resulting statistics are displayed in Fig. 6.

The standard deviations remain within the same order of magnitude independently of the interfacial charge used in the calculation, showing that this is an effect of the experimental conditions and not of the actual charge strength. The standard deviations of the slope estimator are consistently larger than for the offset estimator. However, the actual deviations found in experiments will depend on the range of tilts and thickness measured and will be increased by additional uncertainties caused by noise.

Another observation visible in Fig. 5 is that the variances of the estimators become smaller when tilts far away from the symmetry position are evaluated. This is somewhat expected, as for larger tilts the effects of dynamical diffraction become weaker [22]. However, for larger tilts the slope estimator also becomes biased due to projection effects: It gives systematically smaller field strength for larger negative tilts, while giving systematically larger field strength for larger positive tilts. On a closer look this effect is caused by a broadening and shifting of the QW region due to the projection effect on the tilted QW. This effect can also be mitigated, when the position where the slope is evaluated is shifted with the tilt angle. However, we observe that empirically this shift must be smaller than the geometrically expected amount. This raises the question of how to objectively determine the position where the slope in experimental data is evaluated.

The sensitivity of the slope estimator with respect to spatial resolution was also evaluated. Since the phase profile becomes smoothed in cases of limited resolution, it can be expected that also the estimated field strength becomes biased. Resolution may be limited by two quantities: the width of the area used to calculate the slope, here given by the the width δ of the Gaussian weight, and the reconstruction aperture, here given by the cutoff frequency. The influence of these quantities can be observed in Table I. A general trend of underestimations of the true field strength with decreasing resolution (i.e., increasing rms width δ and decreasing cutoff) is observed. Compared to the observed general variations due to dynamical diffraction, these become only significant when twice the rms width is chosen in the range of the QW width (here 2.25 nm) or the reciprocal of the cutoff is in this range.

Another source of errors occurring with limited resolution becomes more apparent in the simulated profiles in Fig. 7, where also the effects of smaller reconstruction cutoffs are illustrated. When the cutoff is decreased it becomes increasingly more difficult to separate the slope within the QW from the slope of the washed-out phase offset caused by the different material. The raising slope of the material contrast can be easily mistaken for the slope of the QW, resulting in erroneous estimations of the field strengths using the slope

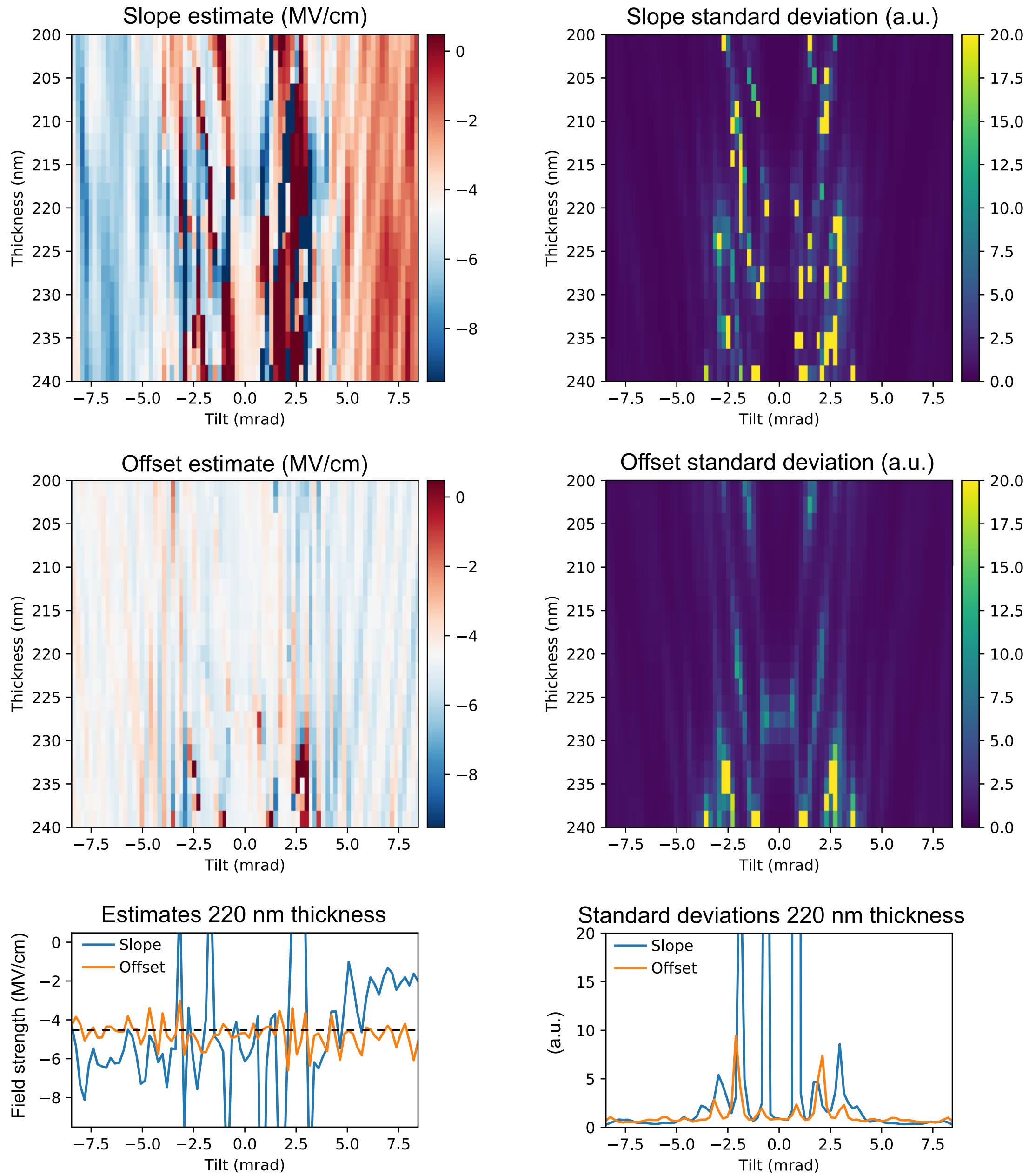

FIG. 5. Left: Estimated electric field strength (given in MV/cm) within the QW for simulated specimen with an interfacial charge of $\sigma_{\text{eff}} = 0.025e/\text{nm}^2$. The expected field strength is $E_{\text{QW}} = -4.524$ MV/cm. Right: Expected standard deviations due to detection noise obtained by error propagation (given in arbitrary units). For better readability the estimates and standard deviations for 220-nm lamella thickness are also plotted in the bottom row.

method. Whether the effect of limited resolution and reconstruction cutoff have a significant influence on the evaluated field strength depends on the conditions of the profile under investigation. For a lamella thickness of 210 nm and zero tilt as in Fig. 7 the effect is very apparent. For a thickness of 220 nm and zero tilt we found no large influence. However, as can be seen from Table I there is an overall influence on the average.

TABLE I. Statistics of the slope method in dependence of center-rms and reconstruction cutoff. An interfacial charge of $\sigma = 0.025e/\text{nm}^2$ was assumed, for which the expected field strength is $E = -4.524$ MV/cm.

Reconstruction cutoff (1/nm)	4.5	4.5	4.5	4.5	1.0	0.5	0.3
Gaussian rms width δ (nm)	0.25	0.50	0.75	1.00	0.50	0.50	0.50
Weighted mean (MV/cm)	−4.4	−4.0	−3.6	−3.2	−4.0	−4.0	−3.5
Weighted standard deviation (MV/cm)	1.6	1.8	1.5	1.2	1.8	2.0	1.6

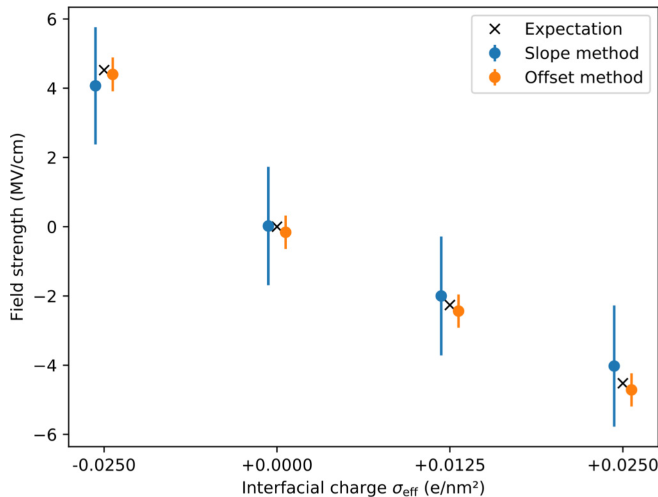

FIG. 6. Weighted average field strength as obtained by the slope and offset methods for four interfacial charges. The weighted standard deviation of the obtained field strength is displayed as error bars. The expected field strength is given by $E_{\text{QW}} = -\sigma_{\text{eff}}/\epsilon_0$. For display purposes the data points are slightly shifted along the abscissa.

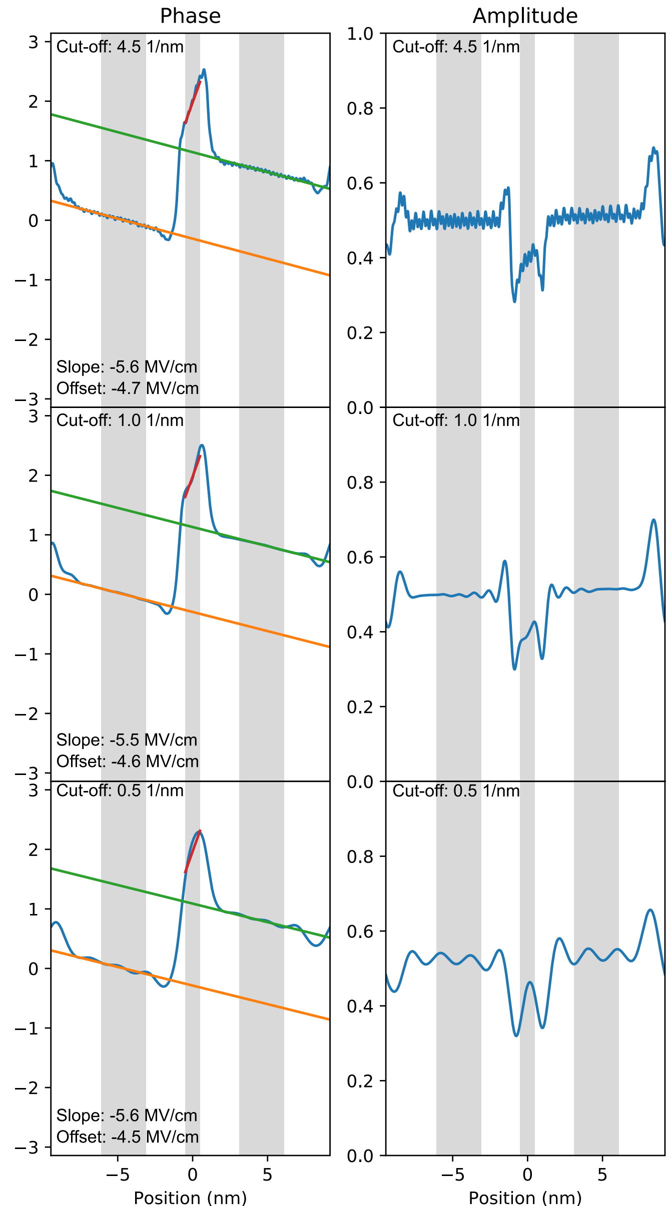

FIG. 7. Simulated profiles for 210-nm-thick lamellas at zero tilt with interfacial charge densities of $\sigma_{\text{eff}} = \pm 0.025e/\text{nm}^2$ for three values of the reconstruction cutoff (expected field strength, $E = -4.524$ MV/cm).

IV. DISCUSSION

A large variation of the evaluated field strength values can be seen with variation of the diffraction conditions and estimator method. For the evaluation of a single orientation this is a systematic error, which can be significantly larger than the statistical error calculated for the individual measurements due to detection noise. Nevertheless, when the experiment is conducted over a sufficient number of beam tilts, the estimated average field strength asymptotically reaches the true value, which means the estimators are statically not biased.

The offset method turned out to be more robust than the slope method. This can be seen in the far smaller standard deviations of the offset estimated values compared to the slope estimated values. While the diffraction effects become less detrimental when larger tilt angles are probed, the imaged QW also becomes broader due to projection effects. Since the position where the slope is estimated must be chosen to some extent objectively in experimental holograms, this causes a significant additional bias for the slope estimation. The slope method also becomes biased when the QW itself is not well resolved anymore; thus it is important to perform such field measurements using the slope method only, when the holograms are not limited by instrumental resolution or too-small reconstruction masks.

The offset method assumes that there is only negligible band bending in the matrix within the range of a few nanometers close to the QW. This might be not necessarily true in a highly doped specimen, where the interfacial charges are effectively screened by the carriers. The offset method also requires knowledge about the width of the QW. Here, we always assumed it is known well enough, since we assume it most times can be obtained from accompanying high-resolution measurements with one-monolayer accuracy, i.e., a relative error of less than 10%. Also the specimen thickness can only be determined with limited precision and accuracy [21] (also see Ref. [46] for a discussion of intricate details of thickness estimation from the mean free path). However, compared to the limited accuracy due to diffraction effects and sensitivity to evaluation position these two additional error sources are negligible in the present case.

While not in the scope of this paper we feel obliged to mention a few more sources of experimental misinterpretations. In principle both estimators (6) and (7) only evaluate the field strength projected over the specimen thickness. This is converted here to an electric field strength by division through the specimen thickness t. So technically the resulting field strength is the average field strength over the thickness. However, this neglects any field variations over the thickness, e.g., due to surface damages from specimen preparation or any band bending due to additional surface charges and/or states. This misinterpretation between thickness-averaged quantities

and bulk quantities was already often discussed in the literature, e.g., under the name of dead layers [18–20]. A further misinterpretation is the influence of the beam itself. The high energetic electrons easily generate electron-hole pairs within the semiconductor, which then change the electrostatic energy landscape within the specimen in dependence on doping levels and how any currents can flow within or around the specimen [20,21]. Thus the situation during the measurement is often not the same as the lower excitation conditions found during device operation. Eventually, the specimen itself degrades under the influence of the electron beam [20,47] and the indium within the QW may segregate [48].

Also it is generally energetically favorable to screen the induced interfacial charges by free carriers, which will also decrease the field strength [1,3]. However, this is expected to have a larger influence on thicker QWs as well as highly doped samples. Also a compensation of the polarization-induced charges by interfacial defect charges is energetically favorable, and will reduce the field strength [1].

V. CONCLUSION

Strong deviations between field strengths obtained under different conditions are found within the conducted simulations. From this three guidelines for accurate results of electric field measurements in QWs can be formulated:

(1) When dynamic diffraction conditions cannot be avoided due to geometric constraints, measurements under various beam tilts should be performed in order to mitigate the dynamical influences. Once the microscope is set up for holographic measurements, usually small beam tilts are easily applied.

(2) If possible, estimate the field strength from the offset step found across the QW in the GaN's matrix potential.

(3) Conduct the experiment with sufficient spatial resolution; e.g., use aberration corrected setups. This also reduces beam tilt constraints due to lens aberrations.

Statistical errors due to detection noise in general underestimate systematical errors caused by dynamical diffraction, resolution-limiting effects, and details of the evaluation method. Reports of electrical field measurements from QWs made by EH should at least contain detailed information about specimen thickness, resolution (reconstruction apertures), evaluation methods, electron dose rate, exact diffraction conditions (specimen orientation), and electrical grounding. Previous measurements found in the literature often miss such details, making the postassessment of these measurements difficult. It should be taken care that these details are always included in future publications.

ACKNOWLEDGMENTS

This investigation arose from discussions within the framework of the Deutsche Forschungsgemeinschaft core facility project "BerlinEM Network," which is gratefully acknowledged.

[1] O. Ambacher, J. Majewski, C. Miskys, A. Link, M. Hermann, M. Eickhoff, M. Stutzmann, F. Bernardini, V. Fiorentini, V. Tilak, B. Schaff, and L. F. Eastman, J. Phys.: Condens. Matter **14**, 3399 (2002).
[2] V. Fiorentini, F. Bernardini, and O. Ambacher, Appl. Phys. Lett. **80**, 1204 (2002).
[3] V. Fiorentini, F. Bernardini, F. Della Sala, A. Di Carlo, and P. Lugli, Phys. Rev. B **60**, 8849 (1999).
[4] R. Cingolani, A. Botchkarev, H. Tang, H. Morkoç, G. Traetta, G. Coli, M. Lomascolo, A. Di Carlo, F. Della Sala, and P. Lugli, Phys. Rev. B **61**, 2711 (2000).
[5] C. X. Ren, Mater. Sci. Technol. **32**, 418 (2016).
[6] J. P. Ibbetson, P. T. Fini, K. D. Ness, S. P. DenBaars, J. S. Speck, and U. K. Mishra, Appl. Phys. Lett. **77**, 250 (2000).
[7] H. Lichte and M. Lehmann, Adv. Imaging Electron Phys. **123**, 225 (2002).
[8] M. R. McCartney, F. A. Ponce, J. Cai, and D. P. Bour, Appl. Phys. Lett. **76**, 3055 (2000).
[9] J. S. Barnard and D. Cherns, J. Electron Microsc. **49**, 281 (2000).
[10] D. Cherns, H. Mokhtari, C. Jiao, R. Averbeck, and H. Riechert, J. Cryst. Growth **230**, 410 (2001).
[11] J. Cai and F. A. Ponce, J. Appl. Phys. **91**, 9856 (2002).
[12] M. Stevens, A. Bell, M. R. McCartney, F. A. Ponce, H. Marui, and S. Tanaka, Appl. Phys. Lett. **85**, 4651 (2004).
[13] C. McAleese, P. M. F. Costa, D. M. Graham, H. Xiu, J. S. Barnard, M. J. Kappers, P. Dawson, M. J. Godfrey, and C. J. Humphreys, Phys. Status Solidi B **243**, 1551 (2006).
[14] L. Zhou, D. A. Cullen, D. J. Smith, M. R. McCartney, A. Mouti, M. Gonschorek, E. Feltin, J. F. Carlin, and N. Grandjean, Appl. Phys. Lett. **94**, 121909 (2009).
[15] L. Zhou, M. Gonschorek, E. Giraud, E. Feltin, J. F. Carlin, N. Grandjean, D. J. Smith, and M. R. McCartney, Appl. Phys. Lett. **101**, 251902 (2012).
[16] L. Zhou, E. Dimakis, R. Hathwar, T. Aoki, D. J. Smith, T. D. Moustakas, S. M. Goodnick, and M. R. McCartney, Phys. Rev. B **88**, 125310 (2013).
[17] B. Haas, J.-L. Rouvière, V. Boureau, R. Berthier, and D. Cooper, Ultramicroscopy **198**, 58 (2019).
[18] W. D. Rau, P. Schwander, F. H. Baumann, W. Höppner, and A. Ourmazd, Phys. Rev. Lett. **82**, 2614 (1999).
[19] A. C. Twitchett, R. E. Dunin-Borkowski, and P. A. Midgley, Phys. Rev. Lett. **88**, 238302 (2002).
[20] J. B. Park, T. Niermann, D. Berger, A. Knauer, I. Koslow, M. Weyers, M. Kneissl, and M. Lehmann, Appl. Phys. Lett. **105**, 094102 (2014).
[21] D. Cooper, J. Phys. D **49**, 474001 (2016).
[22] Z. Gan, M. DiNezza, Y.-H. Zhang, D. J. Smith, and M. R. McCartney, Microsc. Microanal. **21**, 1406 (2015).
[23] W. Qian, M. Skowronski, and G. S. Rohrer, Mater. Res. Soc. Symp. Proc. **423**, 475 (1996).
[24] A. Polian, M. Grimsditch, and I. Grzegory, J. Appl. Phys. **79**, 3343 (1996).
[25] *Properties of Advanced Semiconductor Materials GaN, AlN, InN, BN, SiC, SiGe*, edited by M. Levinshtein, S. Rumyantsev, and M. S. Shur (Wiley, New York, 2001).

[26] K. Kim, W. R. L. Lambrecht, and B. Segall, Phys. Rev. B **53**, 16310 (1996).
[27] M. Schowalter, A. Rosenauer, J. T. Titantah, and D. Lamoen, Acta Crystallogr. Sect. A **65**, 227 (2009).
[28] Y.-N. Xu and W. Y. Ching, Phys. Rev. B **48**, 4335 (1993).
[29] A. S. Barker and M. Ilegems, Phys. Rev. B **7**, 743 (1973).
[30] See Supplemental Material at http://link.aps.org/supplemental/10.1103/PhysRevB.103.075306 for more details.
[31] U. W. Pohl, *Epitaxy of Semiconductors*, Graduate Texts in Physics Vol. 1 (Springer, Berlin, 2013).
[32] J. D. Eshelby and R. E. Peierls, Proc. R. Soc. London A **241**, 376 (1957).
[33] A. Maltsi, T. Niermann, T. Streckenbach, K. Tabelow, and T. Koprucki, Opt. Quantum Electron. **52**, 257 (2020).
[34] J. M. Cowley and A. F. Moodie, Acta Crystallogr. **10**, 609 (1957).
[35] E. J. Kirkland, *Advanced Computing in Electron Microscopy*, 2nd ed. (Springer, Berlin, 2010).
[36] T. Niermann and M. Lehmann, J. Phys. D: Appl. Phys. **49**, 194002 (2016).
[37] T. Niermann, Phys. Rev. B **100**, 144305 (2019).
[38] T. Niermann, PyTEM: Python-based TEM image simulation and processing toolkit, http://www.pytem.org.
[39] O. Ambacher, J. Phys. D **31**, 2653 (1998).
[40] F. Bernardini, V. Fiorentini, and D. Vanderbilt, Phys. Rev. B **56**, R10024 (1997).
[41] F. Bernardini and V. Fiorentini, Phys. Rev. B **64**, 085207 (2001).
[42] F. Bernardini and V. Fiorentini, Phys. Rev. B **65**, 129903(E) (2002).
[43] F. Lenz, Optik **79**, 13 (1988).
[44] F. Röder, A. Lubk, D. Wolf, and T. Niermann, Ultramicroscopy **144**, 32 (2014).
[45] K. Song, C. T. Koch, J. K. Lee, D. Y. Kim, J. K. Kim, A. Parvizi, W. Y. Jung, C. G. Park, H. J. Jeong, H. S. Kim, Y. Cao, T. Yang, L.-Q. Chen, and S. H. Oh, Adv. Mater. Interfaces **2**, 1400281 (2015).
[46] F. Kern, D. Wolf, P. Pschera, and A. Lubk, Ultramicroscopy **171**, 26 (2016).
[47] S. Yazdi, T. Kasama, M. Beleggia, M. S. Yekta, D. W. McComb, A. C. Twitchett-Harrison, and R. E. Dunin-Borkowski, Ultramicroscopy **152**, 10 (2015).
[48] C. J. Humphreys, Philos. Mag. **87**, 1971 (2007).